Research Article Vol. 32, No. 23 / 4 Nov 2024 / Optics Express 40783
Optics EXPRESS

3D coherent single shot lidar imaging beyond coherence length

ATABERK ATALAR,* CHRISTIAN JOSEPH MARGISON, MUSTAFA MERT BAYER, XUN LI, OZAN BERK BOYRAZ, AND OZDAL BOYRAZ

Department of Electrical Engineering and Computer Science, University of California, Irvine, California 92697, USA
aatalar@uci.edu

Abstract: Advancements in remote sensing and autonomous vehicle technologies made lidars equally important for unmanned objects alongside cameras. Therefore, precise 3D lidar imaging and point cloud generation have become important subjects. Although existing coherent lidar technologies provide precise imaging results, the spectral linewidth of the laser sources becomes a key limitation over long distances as it defines the maximum detection range. Here, we present long-distance 3D lidar imaging which removes the coherence length limitations and therefore the necessity of high-coherence laser sources. Mainly, we generate optical sidebands, by modulating a continuous wave (CW) laser source with multiple radio-frequency (RF) tones. Then, using our own post-processing and triangulation methods, we use the relative phase changes between the sidebands which are free from laser phase noise to determine the target distance. We prove that the multi-tone coherent Lidar technique can perform precise 3D imaging and point cloud generation of various targets at sub-10pW optical power reception and distances up to ~12× beyond the coherence length of the CW laser employed in the lidar architecture. Overall, it is demonstrated that coherence length restriction is removed by the suggested method, which makes precise long-distance 3D lidar imaging possible, particularly for applications such as spacecraft and aerial coherent lidars.

1. Introduction

Light detection and ranging (lidar) is an attractive technology with potential implementations in various fields, such as self-driving cars [1–4], unmanned aerial vehicles (UAVs), satellites [5,6], and environmental studies [7,8]. Rapid advancements in these areas have resulted in high demand for long-distance and high-resolution imaging and ranging capabilities for lidar systems, especially in applications where the accuracy and the precision of the generated point cloud of the environment have crucial importance, such as topographical imaging [9,10], remote object detection, oceanographic and atmospheric surveillance [11–13], archeology [14] and proximity sensing for accident prevention [15]. Lidar imaging is commonly achieved by using either pulse time-of-flight (PToF) lidars which uses the time it takes for a light pulse to leave the source and reflect back to the detector from the environment to determine the distance information [16–18] or frequency-modulated continuous-wave (FMCW) [19–21] lidars which utilize the phase or the frequency information extracted from radio frequency (RF) beat tones generated through optical interference at the detector between a frequency or phase swept chirped echo signal from a target and a reference signal to perform ranging. However, coherent lidar techniques have an inherent limitation in measurement range caused by the linewidth (Δf) (i.e. the phase noise) of the laser which affects all systems regardless of the method they are based on [22,23]. The reason is the laser coherence length, $L_{coh} = \frac{c}{\pi \Delta f}$, which leads to error accumulation due to the phase noise [24–26]. For many practical applications, mitigating this limitation with narrow

#529563 https://doi.org/10.1364/OE.529563
Journal © 2024 Received 8 May 2024; revised 11 Oct 2024; accepted 14 Oct 2024; published 25 Oct 2024

Optics EXPRESS

linewidth, high power, and frequency sweeping lasers is not a viable option due to high costs. Previously, we proposed and demonstrated single-point range detection and velocimetry by using a new CW coherent Lidar technology that overcomes the limitations of coherent length. The proposed technique employs a CW laser modulated by multiple phase-locked RF frequencies. Range information is extracted by comparing relative phase changes after coherent detection and using accompanying signal processing algorithms to eliminate the error accumulation due to the phase noise of the laser. To date, in a benchtop experimental demonstration, we have shown the cm level range accuracy of single point range measurements from highly reflective targets at distances that are more than 500× longer than the laser coherence length corresponding to 9 m [27–34].

Here, we present 3D lidar imaging at 12× the laser coherence length (950 m) of multiple objects with varying surface qualities and reflection dynamics, such as Lambertian, quasi-Lambertian, and quasi-specular [35], with collected return optical power as low as 10pW simulating real use cases. In addition, we compare imaging results of similar scenes at distances less than the laser coherence length to demonstrate the immunity of the multi-tone coherent lidar technique to the effects of phase noise when the coherence length is exceeded.

Finally, the measurement consistency and resolving capabilities were shown through the surface scan of slanted targets again from a long distance. In addition, over the slanted target surfaces, the actual slope was compared to the extracted slope information from the imaging results. Through experiments, we demonstrate that the multi-tone coherent lidar method can accurately produce 3D images of targets with a range resolution of <3 cm at distances ranging from 3 m to ~11.4 km (free-space equivalent, limited by the equipment availability) with as low as <10pW received optical power levels and ~1.63 cm average measurement error. Finally, we show that our system can detect the slope of a target along a 31 cm point-to-point distance with 2.98 degrees error after ~7.6 km in fiber and 3 m free space propagation distance.

2. Methodology

2.1. Experimental setup

Figure 1 shows the schematic of the experimental setup constructed using widely available optical components optimized at 1550 nm, in order to evaluate the multi-tone coherent lidar imaging performance at distances less and greater than the laser coherence length. A tunable external-cavity laser tuned at 1550 nm is used as a continuous wave coherent light source outputting ~50 mW. It has a spectral linewidth of 100kHz which corresponds to a coherence length of ~950 m. Subsequently, a two-by-two 50/50 fiber coupler is used to split the light into two branches of equal optical power. Of the two branches, one branch is unmodulated and used as a reference local oscillator (LO) which is utilized for optical heterodyne detection. The other branch functions as the measurement arm of the system and is used as the transmitter. The measurement arm is amplitude modulated using a 10 GHz electro-optic modulator (EOM) to realize stable RF sidebands on the optical carrier that are used to extract range information based on relative phase changes between the RF tones in post-processing. A Tektronix AFG3102 arbitrary function generator is used as a master reference oscillator for the system and outputs a continuous 10 MHz square waveform. Two Windfreak Technologies SynthHD (v2) RF synthesizers generate four RF modulation tones, which are set to be 510, 710, 890, and 950 MHz while using the 10 MHz reference signal as an external trigger. By using the same signal as a reference for both synthesizers, we can realize synchronous initial phases and a common 10 MHz sub-harmonic for all tones generated through phase locking. As a result, the need to calibrate the data processing algorithm for the initial phase states of each tone at generation is removed. Following the EOM, to realize distances beyond the laser coherence length, a standard ~7.6 km SMF fiber spool is added to the measurement arm, which creates a greater propagation distance. However, to realize higher transmission power before free space propagation and to avoid nonlinearities caused by

Optics EXPRESS

high optical power within the fiber, an additional EDFA (Civil Laser EDFA-HP-C-BA-33-M) is used to amplify the optical power to ~200 mW at transmission. Notably, the EDFA does not have a beneficial impact on the laser coherence length and is only used to realize higher transmission power levels. The light is then sent to the target through a collimator with 0.5 cm and 2.5 cm beam diameters on the target surfaces as a result of the beam divergence due to the aperture-target distance. It should be noted that the light propagation in optical fiber is not a perfect equivalent of free space and both scenarios require different approaches in theory and application, as additional losses and atmospheric effects degrade system performance by causing phase distortions impacting high frequency modulation tones [36–38]. Further study and analysis are required to properly assess these effects on PB-MTCW lidar systems. While it is stated that the total free space equivalent distance with the fiber spool reaches up to ~11.4 km it is used to emphasize that our multi-tone coherent lidar system can successfully perform high range accuracy, dense point cloud imaging well beyond the laser coherence length using targets with varying reflection dynamics as well.

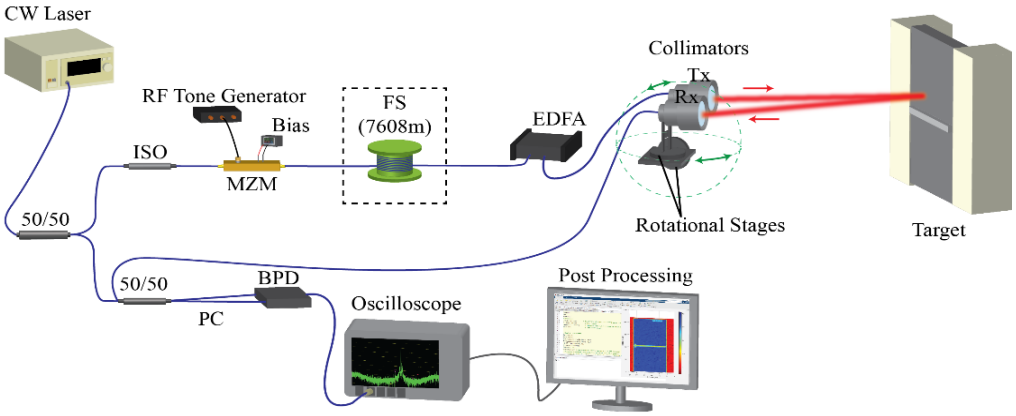

Fig. 1. Experimental layout of the multi-tone coherent lidar imaging system

Due to the sensitivity and lack of time gating in the system, isolation of the transmitter and receiver branches is essential, requiring physical separation of transmitter and receiver paths to prevent back reflection of optical components (i.e., end of fiber cores, collimator lens) which would interfere with distance measurements. Accordingly, in this experiment, a bistatic lidar design is utilized, where a separate collimator is used to collect the echo light from the environment. Additionally, optics were selected such that parameters affecting lateral resolution such as, beam divergence, spot size, and pointing accuracy, have minimal impacts on our imaging results. The collected light is combined with the reference local oscillator branch by using a 2×2 50/50 coupler to realize optical beating. The combined return light and reference local oscillator are guided to a balanced photodetector (BPD) (Thorlabs PDB781CAC) for optical heterodyne detection. A BPD is used to realize a higher SNR with low detection powers. The output signal from the BPD is sampled by a digitizing oscilloscope (Tektronix DPO 71604) at a 6.25 GSPS sampling rate with a 100μs time window. For the single-frame scan results presented in this paper, no specific optimization for scan time or time window size is applied. However, for continuous-high frame rate and denser point cld scans, using a short time window becomes a very important factor. For a 100μs time window with a 1,000,000-point scan, the completion time becomes 100 seconds for one frame (excluding any delays caused by the system itself) which is equal to 0.01 FPS. In multi-tone lidar theory, the time window for data acquisition is limited by the smallest tone frequency used in the experiment. That is, for the tone frequency of 510 MHz, a ~2 ns time window would be enough. For the same example case given previously, the

Optics EXPRESS

completion time becomes 2 ms, and the frame rate exceeds 100 FPS. For imaging with a 1µs time window that accommodates 10 MHz clock frequency and higher tones as presented in the previous work, we anticipate 1FPS [27].

2.2. Data processing

The collected data after each scan was transferred to a local PC for range information extraction and point cloud image construction. Data processing is done using our novel triangulation algorithm. The theory and the mathematical background have been presented previously in detail. A more in-depth explanation about the triangulation algorithm and the post-processing methodology can be found in [27,28,34]. A brief explanation of the process is given as follows. After the echo signal (E_m) travels back from the target and is beat with the unmodulated local oscillator (E_{LO}.) signal through the 2×2 50/50 coupler, the electric field of the resultant beating signal is converted into the detector photocurrent to achieve coherent detection as given in Eq. (1).

$$\begin{aligned} I_{PD} = {} & RA_0^2\alpha_f^2\beta + \frac{3RA_0^2\alpha_m^2\alpha_f^2(1-\beta)}{16} + \frac{RA_0^2\alpha_m\alpha_f^2\sqrt{\beta}\sqrt{1-\beta}}{\sqrt{2}}\cos\left(\omega_0\frac{2L_m}{c}+\Phi(t,\tau)\right) \\ & - \frac{RmA_0^2\alpha_m\alpha_f^2\sqrt{\beta}\sqrt{1-\beta}}{2\sqrt{2}}\left[\begin{array}{l}\sum_{i=1}^{N}\cos\left(\omega_i t+(\omega_0+\omega_i)\frac{2L_m}{c}+\phi_i^{RF}+\Phi(t,\tau)\right) \\ +\sum_{i=1}^{N}\cos\left(\omega_i t-(\omega_0-\omega_i)\frac{2L_m}{c}-\phi_i^{RF}+\Phi(t,\tau)\right)\end{array}\right] \\ & + \frac{RmA_0^2\alpha_m^2\alpha_f^2(1-\beta)}{8}\left[\begin{array}{l}\sum_{i=1}^{N}\cos\left(\omega_i t+\omega_i\frac{2L_m}{c}+\phi_i^{RF}\right) \\ +\sum_{i=1}^{N}\cos\left(\omega_i t+\omega_i\frac{2L_m}{c}-\phi_i^{RF}\right)\end{array}\right] \\ & + \frac{Rm^2A_0^2\alpha_m^2\alpha_f^2(1-\beta)}{8}\sum_{i=1}^{N}\cos\left(2\omega_i t+\omega_i\frac{4L_m}{c}\right) \end{aligned} \tag{1}$$

where ω_0 and ω_i represent the carrier frequency and the i^{th} modulation frequency of N total applied modulation tones, respectively. The laser phase noise difference between local oscillator and the measurement arms is shown as $\Phi(t,\tau)$. The initial phases of the tones which are locked to a fixed value are indicated by ϕ_i^{RF}. Additionally, the parameters such as electric field amplitude, modulation depth, the coupling coefficient of the fiber coupler, optical losses in fiber and the scattering loss are shown as A_0, m, β, α_f and α_m.

$$2A_i\cos\left(\frac{2L_m}{c}\omega_0+\phi_i^{RF}\right)\cos\left(\omega_i t+\frac{2L_m}{c}\omega_i+\Phi(t,\tau)\right) \tag{2}$$

After DC and high scattering loss terms are ignored, the individual tones are defined as shown in Eq. (2) where A_i defines the amplitude of the tone. The post-processing algorithm RF mixes each tone with each other at frequencies ω_i and ω_j ($i \neq j$) and generates phase and amplitude noise-free intermediate frequencies (IF) ($A_iA_j\cos(\Delta\omega_{i,j} \pm \Delta\phi_{i,j})$) that contain the range information as $L_m = (2\pi n + \Delta\phi_{i,j})c/\Delta\omega_{i,j}$ where n is an integer. Multiple RF tones used in the system enable precise target location by sweeping the n values and therefore calculating L_m values for each $\Delta\omega_{i,j}$. The obtained values for L_m are then put into a matrix $M_{k,l}$ where k is set to be the sweeping limit for n and l is the available combinations of $\Delta\omega_{i,j}$. Finally, the standard deviation of the values at each row is calculated using $\sigma_k = \sqrt{\frac{\sum_{r=1}^{l}(M_{k,r}-\bar{M}_k)^2}{l}}$ where $\bar{M}_k$ represents the mean value of the kth row. The distance information on the row with the minimum standard deviation is then accepted as the actual L_m. It should be noted that over long distances, a

Optics EXPRESS

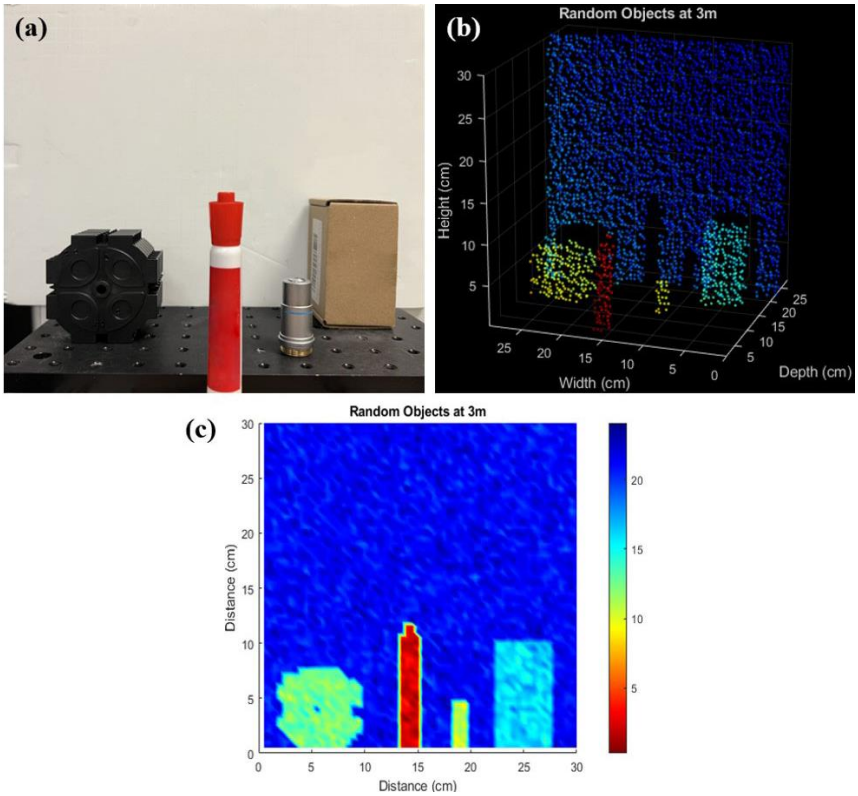

Fig. 2. Imaging results of random objects at 3 m. (a) Scanned target. (b) Point cloud image of the target. (c) Surface plot of the target.

phenomenon called unambiguity length occurs as a repetition of ranging results. In our system, it manifests itself according to $L_{rep} = \frac{2\pi c}{\omega_{GCD}}$ where ω_{GCD} represents the greatest common divisor of the IF tone frequencies and it is calculated as 30 m. The demonstrated experiments are either closer than 30 m or at distances within 30 m after n^{th} repetition along the measurement range. Therefore, the results were not affected by the unambiguous length. After extracting the distance information for each pixel along the target surfaces, an n by m matrix is constructed by matching the pixel locations with the ranging data. By doing so, target dimensions are obtained in 3-dimensional Cartesian coordinates. Then, a conversion to spherical coordinates is applied to obtain the pixel locations and the ranging data as $R = (r, \theta, \phi)$. Once the coordinate system is constructed, the algorithm produces the point cloud data and then a series of low-pass filters are applied to enhance the appearance without changing the information. Finally, the image is generated on MATLAB using built-in functions.

3. Results and analysis

Five separate test cases were used in order to test the performance of our system at distances greater and less than the coherence length. Accordingly, multiple tests were performed while scanning the same scene with an additional fiber spool added to extend the measurement distance. During image processing, the closest target surface was scaled to be the zero point to show the range resolution over long distances.

The first test case was a scan of arbitrary objects made of different materials such as plastic, cardboard, and metal placed at different locations with distances 2.5 ± 0.5 cm in between each

Optics EXPRESS

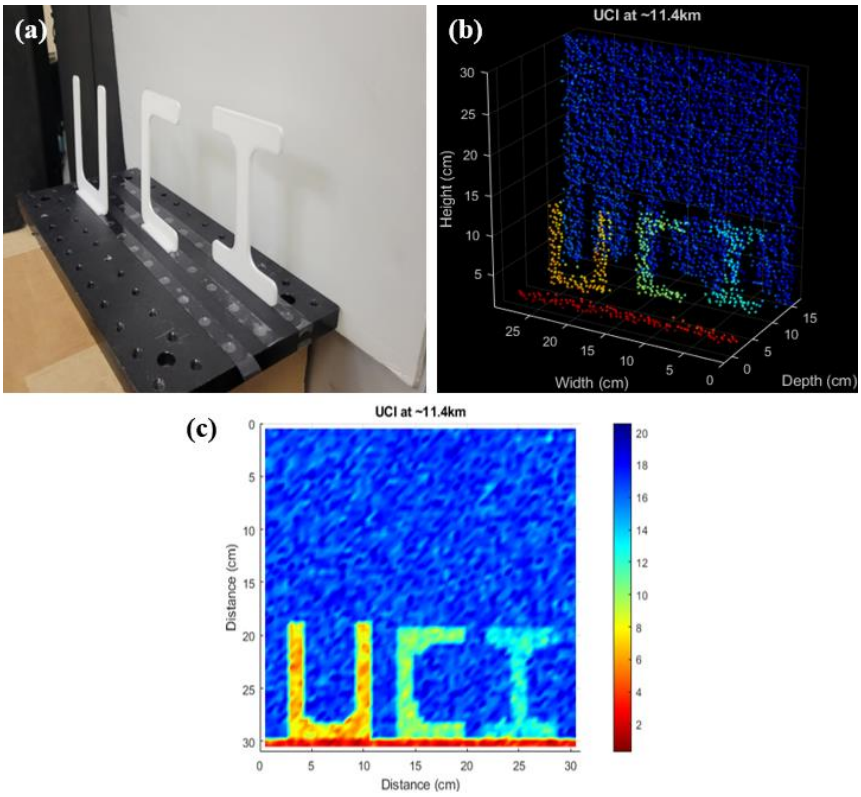

Fig. 3. Imaging results of U, C, and I at 11.4 km. (a) Scanned target. (b) Point cloud image of the target. (c) Surface plot of the target.

object in front of a white cardboard background to assess the performance with different reflection coefficients and surface qualities at a total free space distance of ~3 m. A 60px x 60px scan was conducted with 0.5 cm between each scanning spot, revealing a 30 cm x 30 cm scan area. The total depth of the target was measured with a ruler to be ~21 cm. Figure 2(a) shows the actual target and Fig. 2(b) is the lidar point cloud image generated after scanning with target dimensions and Fig. 2(c) is the surface plot. The received optical power reflected from the target was measured to be ~50pW. It can more clearly be seen in Fig. 2(c) that each object was resolved accurately at their respective positions, which shows a range resolution of <3 cm. Finally, the precision of range is found to be $\alpha =\sim 1.19$ cm by calculating the standard deviation of the data points along each target surface. The second case was a scan of 3D printed (PLA+) letters U, C, and I again in front of the same background placed ~2.54 cm away from each other gradually and the front face of the plate where the letters were placed. The print quality was deliberately reduced to have a rough target surface. By doing so, we aimed to see the results of a more realistic reflection pattern similar to any in-field scenery.

In addition, a ~7.6 km fiber spool was added to increase the total propagation distance to a free space equivalent of ~11.4 km with 3 m true free space distance between the lidar aperture and the target, which in total introduces a measurement range 12× longer than the laser coherence length. As before, a 60×60 scan was performed with 0.5 cm between each scanning spot, revealing a 30 cm x 30 cm scan area. The total depth of the target was measured to be ~15 cm. Figure 3(a) shows the actual target and Fig. 3(b) is the lidar point cloud image generated after scanning with actual dimensions and Fig. 3(c) is the surface plot. The received optical power from target

Optics EXPRESS

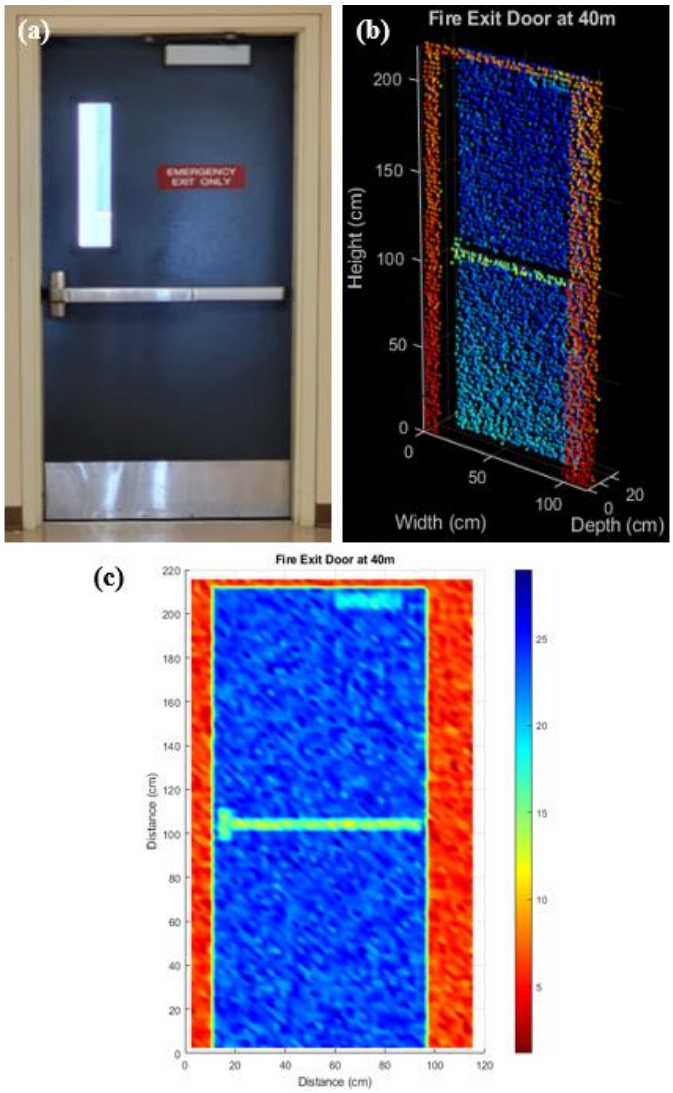

Fig. 4. Imaging results of the fire exit door at 40 m. (a) Scanned target. (b) Point cloud image of the target. (c) Surface plot of the target.

surfaces was measured to be <10pW, which is below the noise level of the optical power meter used in the experiment. Regardless of the coherence length limitation of the laser, each object was resolved accurately at their respective positions which shows a range resolution of <3 cm at ~11.4 km free space equivalent distance. Finally, the ranging accuracy is found to be $\alpha =\sim 1.25$ cm by calculating the standard deviation of the data point along each target surface. The third imaging experiment aims for longer free space distance and larger area scanning. Here we use imaging of a fire exit door located at the end of a hallway which was ~40 m away from the lidar system. In this scenario, the target was inside an 86px x 46px region with each pixel having 2.54 cm in between which resulted in a scan area of 218 cm x 116 cm.

Figure 4(a) shows the actual target and Fig. 4(b) is the lidar point cloud image generated after scanning with actual dimensions and Fig. 4(c) is the surface plot. The total depth of the target between the closest and the furthest surfaces was measured as ~25 cm. The received optical

Optics EXPRESS

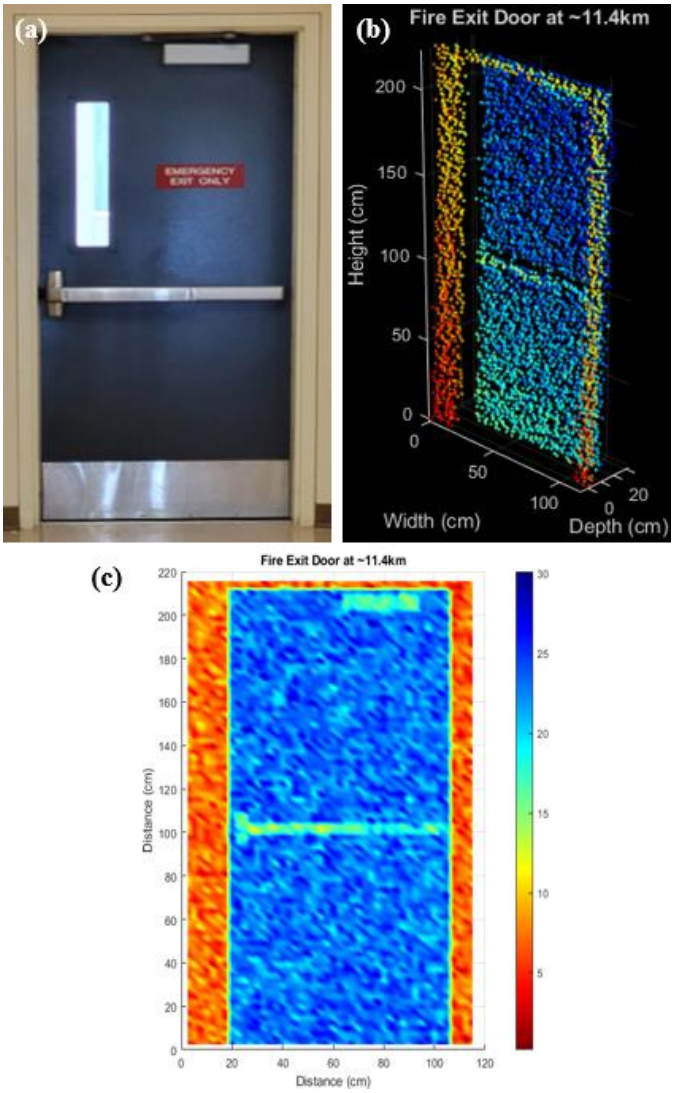

Fig. 5. Imaging results of the fire exit door at 11.4 km. (a) Scanned target. (b) Point cloud image of the target. (c) Surface plot of the target.

power as an echo from target surfaces was measured to be <10 pW, below the sensitivity of the noise floor of the power meter. In Fig. 4(c) it is shown that different surfaces with thickness values ranging from 2.5 cm to 10 cm on the target such as the handle and the stopper were resolved at their respective positions, revealing a resolution <3 cm from 40 m free space distance. Lastly, the ranging precision analysis for this scan scenario was determined to be $\alpha =\sim 1.94$ cm after standard deviation calculation along target surfaces.

The same imaging test was also performed by using the fiber spool to increase the total propagation distance by adding ~7.6 km fiber spool addition to the system, which again increases the total free space equivalent distance to ~11.4 km. The scan dynamics in this scenario were the same as in the fourth case with 86px x 46px scan area with 2.54 cm in between each pixel. Figure 5(a) shows the actual target Fig. 5(b) is the lidar point cloud image generated after scanning with actual dimensions, and Fig. 5(c) is the surface plot. The received optical power from target

Optics EXPRESS

surfaces was again measured to be <10 pW. Figure 5(c) shows the imaging capabilities for different surfaces having various depth values (2.5 cm to 10 cm) on the target at their respective positions with a resolution of <3 cm from 11.4 km free space equivalent distance. The standard deviation for ranging values for this test was calculated to be $\alpha =\sim 2.13$ cm along different parts of the target surface. Small variations in σ might be associated with the thermal fluctuations in the fiber, sampling jitter and noise in the system.

The final test was done to evaluate the ability of the system to achieve accurate ranging and resolve slanted surfaces by generating correct slope values along images. For this purpose, cardboard cutouts of U, C, and I letters placed in front of a background with a slope of $\sim 42 \pm 1$ degrees were used as the target with ~7.6 km fiber addition to the system to increase the propagation distance up to 11.4 km including 3 m true free space distance from lidar aperture. The total scan covered an area of 27px x 96px with ~1.25 cm in between each pixel. However, during image processing, background data was discarded to visually improve the results. Therefore, the presented data covers 18px x 60px which is equal to a 22 cm x 76 cm area. The optical power of the echo signal was again measured as <10pW. Figure 6(a) shows the actual target. Figure 6(b) is the lidar point cloud image generated after scanning with actual dimensions and Fig. 6(c) is the surface plot. The lidar system successfully imaged the target while revealing the gradual change in distance. Additionally, the imaging results on the measured slope and the actual slope are given in Fig. 6(d). The solid yellow line shows the actual slope and the solid white line shows the measured slope as a linear fit on data points over the ZY-plane projection of the target image while revealing the inclination of the target. The variation between the actual and the measured value was recorded as 2.98 degrees.

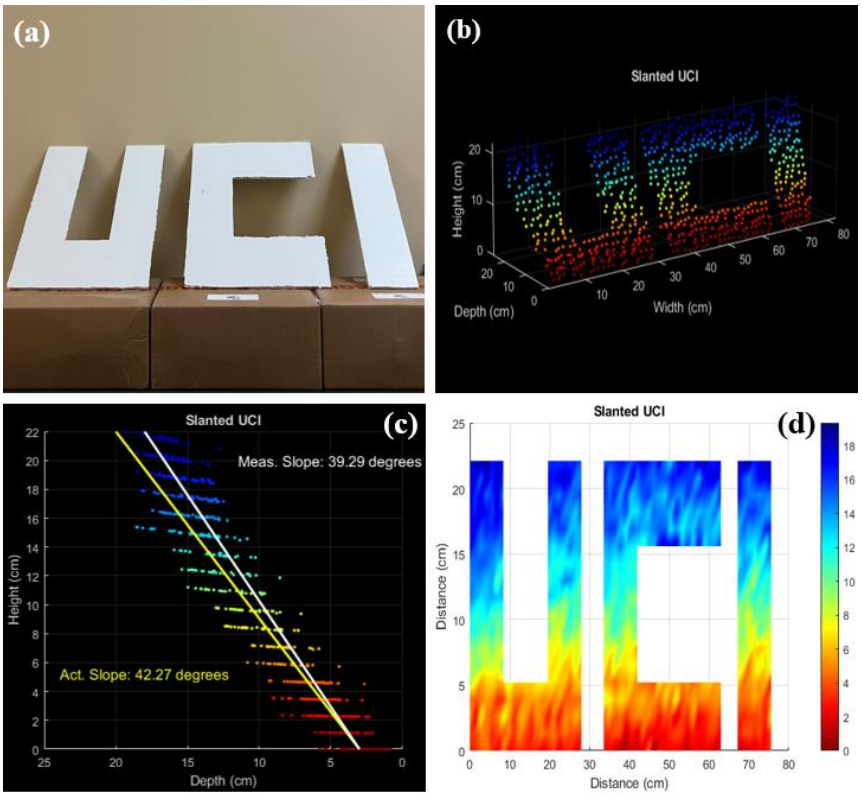

Fig. 6. Imaging results of the ~42degrees slanted U, C and I letters at ~11.4 km (a) Scanned target. (b) Point cloud image of the target. (c) Slope analysis. (d) Surface plot of the target.

Optics EXPRESS

4. Conclusion

We demonstrated the imaging results of our lidar system based on the multi-tone coherent lidar technique, which removes the maximum-range limitations of coherent lidars and makes it possible to achieve imaging beyond the coherence length of the lasers. We presented five test cases using a laser with 100 kHz linewidth equal to a coherence length of 950 m. The maximum and the minimum variations in measurements along target surfaces were found to be α =~2.13 cm at 11.4 km free space equivalent distance and α =~1.19 cm at 3 m. The average variation value, including every scenario, was α =~1.63 cm. Similarly, the average minimum distance resolution was measured as ~2.5 cm. This value is not due to a limitation of our coherent lidar system but having the closest physical distance in between targets around the presented value in experiments. The distance resolution is limited by the sampling rate, jitter, total noises of the system, and surface roughness. We previously showed that we can achieve <1 cm resolution. In addition, a $\sim 42 \pm 1$ degrees slanted target was used to show the system performance with sloped surfaces. The target image was obtained with 2.98 degrees slope error, showing the gradual change in the distance along the target surface. The sensitivity of the detection system is measured to be <10pW. Overall, measurements at different distances with different targets proved the effectiveness of the multi-tone coherent lidar method not only for single point ranging but also surface mapping with sub-nW optical received power levels from targets having non-specular reflection dynamics which is usually the case for long-range satellite or aerial based implementations of lidar systems. However, it should be noted not only the laser coherence length but also the distortive effects on the signal amplitude and phase caused by the propagation medium can limit real-life long-range lidar applications.

Funding. Office of Naval Research (N00014-18-1-2845).

Disclosures. The authors declare that there are no conflicts of interest related to this article.

Data availability. Data underlying the results presented in this paper are not publicly available at this time but may be obtained from the authors upon reasonable request.

References

1. J. Hecht, "Lidar for Self-Driving Cars," Opt. Photonics News **29**(1), 26–33 (2018).
2. C. Urmson, J. Anhalt, D. Bagnell, *et al.*, "Autonomous Driving in Urban Environments: Boss and the Urban Challenge," in *The DARPA Urban Challenge: Autonomous Vehicles in City Traffic*, M. Buehler, K. Iagnemma, S. Singh, *et al.*, eds. (Springer, 2009), pp. 1–59.
3. W. Zhang, "LIDAR-based road and road-edge detection," in *2010 IEEE Intelligent Vehicles Symposium* (2010), pp. 845–848.
4. Q. Zhu, L. Chen, Q. Li, *et al.*, "3D LIDAR point cloud based intersection recognition for autonomous driving," in *2012 IEEE Intelligent Vehicles Symposium* (2012), pp. 456–461.
5. R. H. Couch, C. W. Rowland, K. S. Ellis, *et al.*, "Lidar In-Space Technology Experiment (LITE) - NASA's first in-space lidar system for atmospheric research," Opt. Eng. **30** (1991).
6. L. Wallace, A. Lucieer, C. Watson, *et al.*, "Development of a UAV-LiDAR System with Application to Forest Inventory," Remote Sens. **4**(6), 1519–1543 (2012).
7. A. Nettley, K. Anderson, C. D. Silvey, *et al.*, "Using Terrestrial Laser Scanning And Lidar Data For Photo-Realistic Visualisation Of Climate Impacts At Heritage Sites," Int. Arch. Photogramm. Remote Sens. Spatial Inf. Sci. **XXXVIII-5/W16**, 223–229 (2012).
8. S. A. F. S. A Rahman, K. N. A. Maulud, and H. Hassan, "Leveraging LiDAR for smart cities climate change resilient: A solar potential case study in a developing area," *OP Conference Series: Earth and Environmental Science*1167, 012023 (2023).
9. J. L. Bufton, J. B. Garvin, J. F. Cavanaugh, *et al.*, "Airborne lidar for profiling of surface topography," Opt. Eng. **30**(1), 72 (1991).
10. S. Ullah, P. Adler, M. Dees, *et al.*, "Comparing image-based point clouds and airborne laser scanning data for estimating forest heights," iForest **10**(1), 273–280 (2017).
11. Y. Megahed, A. Shaker, and W. Y. Yan, "Fusion of Airborne LiDAR Point Clouds and Aerial Images for Heterogeneous Land-Use Urban Mapping," Remote Sens. **13**(4), 814 (2021).
12. J. A. Yoder, J. Aiken, R. N. Swift, *et al.*, "Spatial variability in near-surface chlorophyll *a* fluorescence measured by the Airborne Oceanographic Lidar (AOL)," Deep Sea Res., Part II **40**(1-2), 37–53 (1993).
13. J. Hair, C. Hostetler, Y. Hu, *et al.*, "Combined Atmospheric and Ocean Profiling from an Airborne High Spectral Resolution Lidar," EPJ Web Conf. **119**, 22001 (2016).

Optics EXPRESS

14. D. A. White, "LIDAR, Point Clouds, and Their Archaeological Applications," in *Mapping Archaeological Landscapes from Space*, D. C. Comer and M. J. Harrower, eds. (Springer, 2013), pp. 175–186.
15. J. Liu, Q. Sun, Z. Fan, *et al.*, "TOF Lidar Development in Autonomous Vehicle," in *2018 IEEE 3rd Optoelectronics Global Conference (OGC)* (2018), pp. 185–190.
16. Y. Jiang, S. Karpf, and B. Jalali, "Time-stretch LiDAR as a spectrally scanned time-of-flight ranging camera," Nat. Photonics **14**(1), 14–18 (2020).
17. B. Behroozpour, P. A. M. Sandborn, M. C. Wu, *et al.*, "Lidar System Architectures and Circuits," IEEE Commun. Mag. **55**(10), 135–142 (2017).
18. H. Rapp, M. Frank, F. A. Hamprecht, *et al.*, "A theoretical and experimental investigation of the systematic errors and statistical uncertainties of Time-Of-Flight-cameras," Int. J. Intell. Syst. Technol. Appl. **5**(3/4), 402–413 (2008).
19. F. Zhang, L. Yi, and X. Qu, "Simultaneous measurements of velocity and distance via a dual-path FMCW lidar system," Opt. Commun. **474**, 126066 (2020).
20. M. Okano and C. Chong, "Swept Source Lidar: simultaneous FMCW ranging and nonmechanical beam steering with a wideband swept source," Opt. Express **28**(16), 23898–23915 (2020).
21. D. Uttam and B. Culshaw, "Precision time domain reflectometry in optical fiber systems using a frequency modulated continuous wave ranging technique," J. Lightwave Technol. **3**(5), 971–977 (1985).
22. J. Riemensberger, A. Lukashchuk, M. Karpov, *et al.*, "Massively parallel coherent laser ranging using a soliton microcomb," Nature **581**(7807), 164–170 (2020).
23. N. G. Pavlov, S. Koptyaev, G. V. Lihachev, *et al.*, "Narrow-linewidth lasing and soliton Kerr microcombs with ordinary laser diodes," Nat. Photonics **12**(11), 694–698 (2018).
24. J. Morville, D. Romanini, M. Chenevier, *et al.*, "Effects of laser phase noise on the injection of a high-finesse cavity," Appl. Opt. **41**(33), 6980–6990 (2002).
25. C. Henry, "Phase noise in semiconductor lasers," J. Lightwave Technol. **4**(3), 298–311 (1986).
26. Y. Zhou, C. Zheng, Z.-K. Weng, *et al.*, "Effects of a variable linewidth laser and variable linewidth shape laser on coherent FMCW LiDAR," Opt. Continuum **2**(5), 1122–1136 (2023).
27. M. M. Bayer, X. Li, G. N. Guentchev, *et al.*, "Single-shot ranging and velocimetry with a CW lidar far beyond the coherence length of the CW laser," Opt. Express **29**(26), 42343–42354 (2021).
28. M. M. Bayer, A. Atalar, X. Li, *et al.*, "Demonstration of Optical Clock-Free Localization and Navigation (CLAN)," J. Lightwave Technol. **41**(20), 6457–6464 (2023).
29. M. M. Bayer, A. Atalar, X. Li, *et al.*, "Photonics PNT Based on Multi-Tone Continuous Wave Ranging," in *2022 Conference on Lasers and Electro-Optics (CLEO)* (2022), pp. 1–2.
30. M. M. Bayer, B. U. Demirel, A. Atalar, *et al.*, "Optical ranging and localization at beyond the coherence length of lasers," in *AI and Optical Data Sciences IV*, K. Kitayama and B. Jalali, eds. (SPIE, 2023), p. 41.
31. M. M. Bayer, B. U. Demirel, A. Atalar, *et al.*, "Machine-learning-enhanced phase-based multi-tone continuous-wave lidar," Photonic Instrumentation Engineering X **12428**, 26 (2023).
32. M. M. Bayer, A. Atalar, X. Li, *et al.*, "Photonic Localization and Positioning using Multi-Tone Continuous-Wave Ranging Methodology," in *2023 IEEE Aerospace Conference* (2023), pp. 1–7.
33. M. M. Bayer and O. Boyraz, "Ranging and velocimetry measurements by phase-based MTCW lidar," Opt. Express **29**(9), 13552–13562 (2021).
34. M. M. Bayer, "Multi-Tone Continuous-Wave Lidar," phd, University of California, Irvine (2022).
35. Y. Nakajima, T. Sasaki, N. Okada, *et al.*, "LiDAR Measurement Simulator Considering Target Surface Reflection," in (2021).
36. W. O. Popoola and Z. Ghassemlooy, "BPSK Subcarrier Intensity Modulated Free-Space Optical Communications in Atmospheric Turbulence," J. Lightwave Technol. **27**(8), 967–973 (2009).
37. E. Leitgeb, M. Gebhart, P. Fasser, *et al.*, "Impact of atmospheric effects in free-space optics transmission systems," *Proc. SPIE 4976, Atmospheric Propagation*, (30 April 2003).
38. P. T. Dat, A. Bekkali, K. Kazaura, *et al.*, "Studies on characterizing the transmission of RF signals over a turbulent FSO link," Opt. Express **17**(10), 7731–7743 (2009).